

NEW LIMITS ON STERILE NEUTRINOS FROM SUZAKU OBSERVATIONS OF THE URSA MINOR DWARF SPHEROIDAL GALAXY

Michael Loewenstein^{1,2}, Alexander Kusenko^{3,4}, Peter L. Biermann^{5,6,7}

(Received 2008 December 14; Accepted 2009 May 19)

To be published in the Astrophysical Journal Vol. 698, UCL A /08/TEP /32

ABSTRACT

We present results of our search for X-ray line emission associated with the radiative decay of the sterile neutrino, a well-motivated dark matter candidate, in Suzaku Observatory spectra of the Ursa Minor dwarf spheroidal galaxy. These data represent the first deep observation of one of these extreme mass-to-light systems and the first dedicated dark matter search using an X-ray telescope. No such emission line is positively detected, and we place new constraints on the combination of the sterile neutrino mass, m_{st} , and the active-sterile neutrino oscillation mixing angle, θ . Line flux upper limits are derived using a maximum-likelihood-based approach that, along with the lack of intrinsic X-ray emission, enables us to minimize systematics and account for those that remain. The limits we derive match or approach the best previous results over the entire 1–20 keV mass range from a single Suzaku observation. These are used to place constraints on the existence of sterile neutrinos with given parameters in the general case and in the case where they are assumed to constitute all of the dark matter. The range allowed implies that sterile neutrinos remain a viable candidate to make up some (or all) of the dark matter and also explain pulsar kicks and various other astrophysical phenomena.

Subject headings: dark matter { galaxies: dwarf { galaxies: individual (Ursa Minor)

1. INTRODUCTION

The observational evidence that nonbaryonic dark matter comprises most of the mass in the universe is extremely strong, but the nature of dark-matter particles remains a mystery. No particle included in the Standard Model of particle physics has the characteristics required to explain the dark matter. In its original formulation, the Standard Model described all known particles, including neutrinos, which were assumed to be massless. The discovery that neutrinos have mass has forced one to go beyond this minimal model: a modest extension of the Standard Model by gauge singlet fermions can accommodate the neutrino masses. One or more of these gauge-singlet fermions can have Majorana masses below the electroweak scale, in which case they appear as sterile neutrinos in the low-energy theory. If one of the sterile neutrinos has mass in the 1–20 keV range and has small mixing angles with the active neutrinos (as expected), such a particle is a plausible candidate for dark matter (Dodelson & Widrow 1994). The same particle could be produced in a supernova explosion, and its emission from a cooling neutron star could explain the pulsar kicks (Kusenko & Segre 1997; Fuller et al.

2003; Kusenko 2004; Kusenko, Mandal, & Mukherjee 2008), could facilitate core collapse supernova explosions (Fryer & Kusenko 2006; Hidaka & Fuller 2007) and can affect the formation of the first stars (Biermann & Kusenko 2006; Stasielak, Biermann, & Kusenko 2007) and black holes (Munyanza & Biermann 2005, 2006). Therefore, there is a strong motivation to search for signatures of sterile neutrinos in this mass range.

The most promising way to discover (or rule out) relic sterile neutrinos is with the use of X-ray telescopes (XRTs), such as Suzaku. The sterile neutrinos can decay radiatively (Pal & Wolfenstein 1982; Barger et al. 1995) and produce a lighter neutrino and a photon amenable to X-ray observation (Abazajian, Fuller, & Patel 2001; Abazajian, Fuller, & Tucker 2001; Dolgov & Hansen 2002). Since this is a two-body decay, a line is expected in the X-ray spectrum. The dwarf spheroidal galaxies are ideal targets for these observations because of their proximity, high dark matter density (Strigari et al. 2008a), and absence of additional obscuring X-ray sources (see below). The Ursa Minor and Draco dwarf spheroidals are the optimal targets in this class for large field-of-view X-ray spectroscopic investigation, based on their average dark matter surface densities. From XMM-Newton observations of the Ursa Minor dwarf spheroidal, sterile neutrino line flux limits comparable to the best previous constraints were derived (even though strong background arising limited the amount of good observing time to 7 ks (Boyarsky, Nevalainen, & Ruchayskiy 2007)). The Suzaku Observatory (Mitsuda et al. 2007) provides the most sensitive instruments for current searches for weak sterile neutrino radiative decay lines in the 0.5–10 keV bandpass because of its low and stable background (Tawa et al. 2008), and the relatively sharp spectral resolution of its CCD spectrometers

Electronic address: MichaelLoewenstein@nasa.gov

¹ Department of Astronomy, University of Maryland, College Park, MD.

² CRESST and X-ray Astrophysics Laboratory NASA/GSFC, Greenbelt, MD.

³ Department of Physics and Astronomy, University of California, Los Angeles, CA 90095-1547, USA

⁴ Institute for the Physics and Mathematics of the Universe, University of Tokyo, Kashiwa, Chiba 277-8568, Japan

⁵ Max-Planck-Institut für Radioastronomie, Bonn, Germany.

⁶ Department of Physics and Astronomy, University of Bonn, Bonn, Germany.

⁷ Department of Physics and Astronomy, University of Alabama, Tuscaloosa, AL

(Koyama et al. 2007; Nakajima et al. 2008). In this paper, we discuss our analysis of Suzaku observations of the Ursa Minor system, considerably improving on the XMM-Newton constraints; a companion article on the Draco system is in preparation. These represent the first substantial X-ray data of such extremely dark-matter-dominated systems.

1.1. Context

Sterile neutrinos may be produced through non-resonant oscillations, as proposed by Dodelson and Widrow (Dodelson & Widrow 1994), and via various other mechanisms (Dolgov 2002; Shi & Fuller 1999; Shaposhnikov & Tkachev 2006; Kusenko 2006; Kadota 2008; Petraki & Kusenko 2008). A generic prediction is that relic sterile neutrinos must decay into a lighter neutrino and a photon. Since this is a two-body decay of a particle with mass m_{st} , decay photons produce an intrinsically narrow line with energy $E = m_{st}/2$ that can be detected using X-ray spectroscopy (Abazajian, Fuller, & Tucker 2001). While the decay timescale, τ_{st} , greatly exceeds the Hubble time, the emissivity may reach detectable levels in regions of large dark matter concentration. Upper limits on τ_{st} from X-ray observations of the cosmic background (Abazajian & Koushiappas 2006; Boyarsky et al. 2006a; Abazajian et al. 2007), galaxy clusters (Boyarsky et al. 2006b; Riemer-Sørensen et al. 2007; Boyarsky, Ruchayskiy, & Markevitch 2008), and M31 (Watson et al. 2006; Riemer-Sørensen et al. 2007; Boyarsky et al. 2008) may be complemented and improved by observing dwarf spheroidal galaxies (Boyarsky et al. 2006c).

There is no consensus as to whether dark matter is cold or warm based on observations of small-scale structure. Cold and warm dark matter reproduce large-scale structure equally well, but differ in their predictions on scales comparable to the free-streaming length. Ly forest clouds provide a tracer population of the perturbation spectrum on the appropriate (non-linear) scale that may be used to place an upper limit on the free-streaming length (Narayanan et al. 2000), and have been interpreted as implying that the mass of the dark matter sterile neutrino, m_{st} , must be greater than ~ 8 keV (Viel et al. 2008; Boyarsky et al. 2009) for production exclusively by the Dodelson-Widrow (DW) non-resonant mixing mechanism. However, N-body simulations and observations of dwarf spheroidal galaxies imply a lower mass (Gilmore et al. 2007; Strigari et al. 2007a). In scenarios with alternative production mechanisms that do not involve oscillations, sterile neutrinos may effectively be colder, allowing masses as low as 3 keV to be consistent with the Ly observations (Kusenko 2006; Petraki & Kusenko 2008; Petraki 2008). In this case, the photometric and kinematic data from dwarf spheroidal galaxies (Gilmore et al. 2007; Strigari et al. 2007a) can be satisfied by dark matter in the form of sterile neutrinos with mass between 0.5 keV and 1.3 keV (Boyanovsky 2008). Constraints on sterile neutrino parameters may be further relaxed in mixed dark matter models (Palazzo et al. 2007; Boyarsky et al. 2009) and in models where sterile neutrinos are produced in resonant oscillations in the presence of significant lepton asymme-

tries (Shi & Fuller 1999; Laine & Shaposhnikov 2008). Since the sterile neutrino distribution function may substantially deviate from thermal equilibrium (Abazajian 2006a,b; Petraki 2008; Boyanovsky 2008), simple scaling arguments and alterations to the power spectrum (e.g., imposing a cutoff) do not suffice. New large-scale structure formation simulations with the appropriate revisions are required to re-evaluate the constraints from Ly data (Laine & Shaposhnikov 2008; Boyanovsky 2008). Moreover, their interpretation relies on a thorough understanding of the uncertain thermal and ionization evolution of the intergalactic medium, which may be affected by the properties and interactions of dark-matter particles (Birnann & Kusenko 2006; Gao & Theuns 2007; Meiksin 2009). Hence, we present limits solely derived from our X-ray data.

The sterile neutrino mass and the mixing angle determine the rate of radiative decay to active neutrinos and X-ray photons: $\Gamma_{st \rightarrow \nu \gamma} \propto \theta^2 m_{st}^5$. The radiative decay width is equal to (Pal & Wolfenstein 1982)

$$\begin{aligned} \Gamma_{st \rightarrow \nu \gamma} &= \frac{9}{256} \frac{1}{4} \epsilon_{EM} G_F^2 \sin^2 \theta m_s^5 \\ &= \frac{1}{1.8 \times 10^{31} \text{ s}} \frac{\sin^2 \theta}{10^{-10}} \frac{m_s^5}{\text{keV}^5}; \quad (1) \end{aligned}$$

where $\epsilon_{EM} = 1/137.0$ and $G_F = 1.2 \times 10^{-5} \text{ GeV}^{-2}$.

For a given production mechanism, one may be able to eliminate one of these two parameters by requiring that the total density match that of dark matter in the universe as inferred from observations. However, given the various possible mechanisms for producing sterile neutrinos, and the possibility that sterile neutrinos may account for some (but not all) dark matter (Palazzo et al. 2007), one should keep an open mind and search all the available parameter space in the m_{st} plane.

2. DATA ANALYSIS

2.1. Observations and Initial Reduction

Ursa Minor (OBSID = 802052010) was observed with Suzaku (Mitsuda et al. 2007) between 2007 April 5 18:33:24 and 2007 April 6 8:08:14 (UT) with an on-source exposure time of 70.90 ks, 57.5 (13.4) ks in a 5 × 5 (3 × 3) editing mode (this refers to the pixel area utilized in event identification that is included in the telemetry; see Koyama et al. 2007). At the time of observation, three co-aligned, 17° × 17° field-of-view X-ray Imaging Spectrometer (XIS) CCD cameras (Koyama et al. 2007) (two front-illuminated (FISIS0 and FISIS3) and one back-illuminated (BIXIS1)) were operational. The BIC chip is more sensitive below 1 keV but has a much higher internal background, especially above 7 keV, so that BI and FICCDs complement each other for broad-band studies such as ours. Each XIS lies in the focal plane of an XRT with a 2° half-power diameter (Serlemitsos et al. 2007).

Suzaku guest observers are provided with unfiltered and pre-screened event lists. We initiate our data reduction with the Ursa Minor unfiltered event lists. These underwent Version 2.0.6.13 pipeline processing that, for each event, assigns a pixel quality status, calculates the sky coordinates using the current aspect solution and correcting for spacecraft wobble (Uchiyama et al. 2008), and converts pulse height amplitude (PHA) to PHA In-

variant (PI) values that map to photon energy in a one-to-one manner. Observations were conducted utilizing the space-row charge injection (SCI) technique that reverses the degradation in energy resolution caused by accumulated radiation damage and affects the conversion from the PHA channel to energy (Nakajima et al. 2008). Version 2 pre-processing enables one to properly account for the effect of SCI on instrument characteristics and performance (Uchiyama et al. 2009). We reprocess the unfiltered event files by hand in order to apply updated calibration data and software. Our analysis generally follows the procedures outlined in "The Suzaku Data Reduction Guide,"⁸ as implemented in HEASOFT version 6.5.1⁹. We recalculate PI values and grades, select event grades (0, 2, 3, 4, 6) that correspond to X-ray photon events, filter on pixel status (eliminating bad charge transfer efficiency columns, and rows invalidated by the charge injection process) and select good time intervals (GTI) based on pointing, data and telemetry rates, SAA proximity ($\text{SAA_HXD} = 0; \text{T_SAA_HXD} > 436$ "), and proximity to the Earth's limb and illuminated Earth ($\text{ELV} > 5; \text{DYE_ELV} > 20$ "). In addition, telemetry-saturated frames and calibration source photons are screened out and hot and flickering pixels are removed. Finally, we accept only GTI where the revised geomagnetic cut-off rigidity $\text{COR2} > 4$, thus eliminating intervals with the highest particle background level (Tawa et al. 2008) without compromising overall statistical accuracy (experiments with more stringent criteria $\{ \text{COR2} > 6, \text{COR2} > 8 \}$ yielded consistent results, but with significantly poorer statistics). 55 event files are converted to a 3 × 3 mode format, and merged with the 55 event files.

2.2. Spectral Analysis Procedure

2.2.1. Generation of Spectra and Spectral Response

The extraction region used to create source and particle background spectra is constructed to include the entire detector fields-of-view, excluding an 8° diameter circular region centered on the one bright point source in the field. This radius was found to balance the desires to avoid contamination of the diffuse emission from the wings of the point-spread function and to maximize the statistical accuracy through inclusion of regions dominated by diffuse emission.

The spectral redistribution matrices (rmf) are generated based on the characteristics and configuration of the instruments at the time of observation. The rmf and spectral files are binned to 2048 channels. The effective area functions (arf) are generated via a Monte Carlo ray-tracing program that calculates the efficiency of detecting a photon originating from a specified source geometry and surface brightness distribution within a specified spectral extraction region (Ishisaki et al. 2007). We input 2,000,000 simulation photons per energy bin from a uniform source of radius 20°, cast the spectral extraction regions into detector coordinates, and adopt a single arf file for all components (the Ursa Minor dark matter density is sufficiently at over this radius that any correction to such a component is small). The resulting arf file is

scaled such that the flux calculated for spectral models corresponds to the full 20° circular region.

The spectra from the FI chips, XIS0 and XIS3, are co-added and a weighted XIS0+3 response function calculated.

2.2.2. Background Components

Since dwarf spheroidal galaxies are intrinsically weak X-ray emitters (see below), their X-ray spectra are dominated by internal and astrophysical background components. The XIS background includes contributions from non-X-ray charged particle background (NXB), galactic X-ray background (GXB), and (extragalactic) cosmic X-ray background (CXB).

The NXB component is estimated from observations of the night earth taken in the SCI mode within 150 days of the starting or ending dates of the Ursa Minor observation (Tawa et al. 2008). The NXB event list in that time interval undergoes the identical screening as the source data, is sorted by geomagnetic cut-off rigidity, and weighted according to the cut-off rigidity distribution in the source event file (Tawa et al. 2008). The estimated NXB spectra includes only those events collected in the region on the detector from which the source spectrum is extracted. XIS0 and XIS3 NXB spectra are co-added. The effective NXB spectra exposure times and count rates for the XIS0+3 (XIS1) are 1.1 (0.55) million seconds and 0.062 (0.090) counts per second, respectively, where the count rates are integrated over the 0.45–10.4 (0.45–7.6) keV bandpass (see below).

The GXB may be characterized by a two-temperature thermal plasma (corresponding to halo and local hot bubble contributions) and the CXB by a single power law. We find that this model produces a good global simultaneous $\chi^2 = 1205$ for 1232 degrees of freedom) to the NXB-subtracted, binned, 0.45–10.4 keV XIS0+3 and 0.45–7.6 keV XIS1 spectra (Figures 1 and 2), where the two spectra are fitted by the identical model save for a constant multiplicative factor. Additional components are not required; however, allowing non-solar oxygen abundance does improve the fit. We find that the resulting parameters are consistent with the spectrum extracted from the ROSAT All-Sky Survey¹⁰.

Any intrinsic X-ray continuum is indeed negligible. With a maximum circular velocity $< 30 \text{ km s}^{-1}$ (Strigari et al. 2007a), X-ray emitting gas cannot be bound to the Ursa Minor dwarf spheroidal. We may estimate the emission from unresolved stellar X-ray sources by scaling to the optical luminosity of Ursa Minor ($\sim 3 \times 10^5 L_{\odot}$) using the relation and X-ray spectral parameters in Revnivtsev et al. (2008). There may also be an intermediate mass black hole in Ursa Minor. Based on extensions of the observed correlations of nuclear black hole mass with velocity dispersion (Gebhardt et al. 2000; Ferrarese & Ford 2005; Graham 2008a,b), bulge luminosity or mass (Marconi & Hunt 2003; Haring & Rix 2003; Ferrarese & Ford 2005), or dark matter halo mass (Ferrarese & Ford 2005) in early type stellar systems, one expects $M_{\text{bh}} \sim 300 \text{--} 10^4 M_{\odot}$ (although these correlations may change or break down at low mass (Greene, Ho, & Barth 2008)).

⁸ <http://heasarc.gsfc.nasa.gov/docs/suzaku/analysis/abc/>

⁹ <http://heasarc.gsfc.nasa.gov/docs/software/lheasoft/>

¹⁰ <http://heasarc.gsfc.nasa.gov/cgi-bin/Tools/xraybg/xraybg.pl>

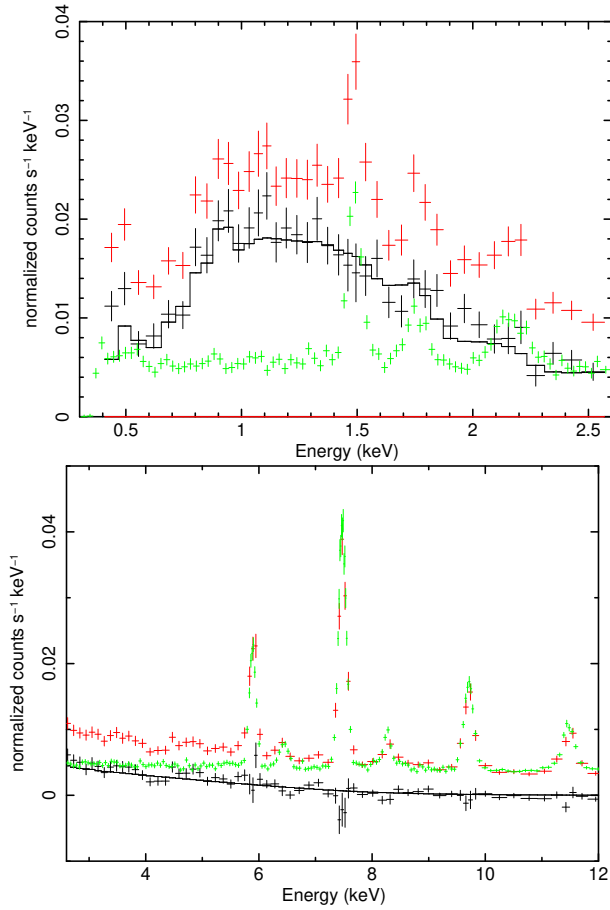


Fig. 1. | Low-energy (< 2.6 keV; above) and high energy (> 2.6 keV; below) XIS0+3 spectra. Shown are total (red symbols), NXB (green symbols), and total NXB (black symbols). The best-fit CXB+GXB model to the NXB-subtracted spectra is shown by the black histogram. The best-fit was obtained by simultaneously fitting the 0.45–10.4 keV XIS0+3 and 0.45–7.6 keV XIS1 spectra; the extension of the model, as well as that of the data, is plotted over the full 0.3–12 keV bandpass.

This mass range is estimated by using the measured Ursa Minor velocity dispersion (Wilkinson et al. 2004) and by considering stellar mass-to-light ratios of $1-3$ (Zaritsky, Gonzalez, & Zabludovskiy 2006) and a dark matter virial mass $10^9 M_{\odot}$. Maccarone, Fender, & Tzioumis (2005) estimate an expected X-ray luminosity of 7×10^{34} erg s $^{-1}$ for $M_{\text{bh}} = 2.3 \times 10^4 M_{\odot}$. We plot the Suzaku spectrum for an index 1.7 power law with $L_{\text{X}} = 3 \times 10^{34}$ erg s $^{-1}$, and an optimistic estimate of the unresolved stellar emission, along with the background-subtracted XIS0+3 spectrum of Ursa Minor in Figure 3.

Typically, in Suzaku extended source spectral analysis (Matsushita et al. 2007; Takei et al. 2007; Tawara et al. 2008; Tokoi et al. 2008; Sato et al. 2008), the estimated NXB is directly subtracted and the source model often extended to include the GXB and CXB (perhaps with a subset of GXB/CXB parameters fixed based on previous observations). One set of “blank-sky” fields may be employed to directly subtract or fix the parameters of these components. The NXB-subtracted spectrum is binned and best fits and confidence levels are derived from χ^2 statistics. Many previous limits on sterile neutrino radiative decay line fluxes are derived employing variations on

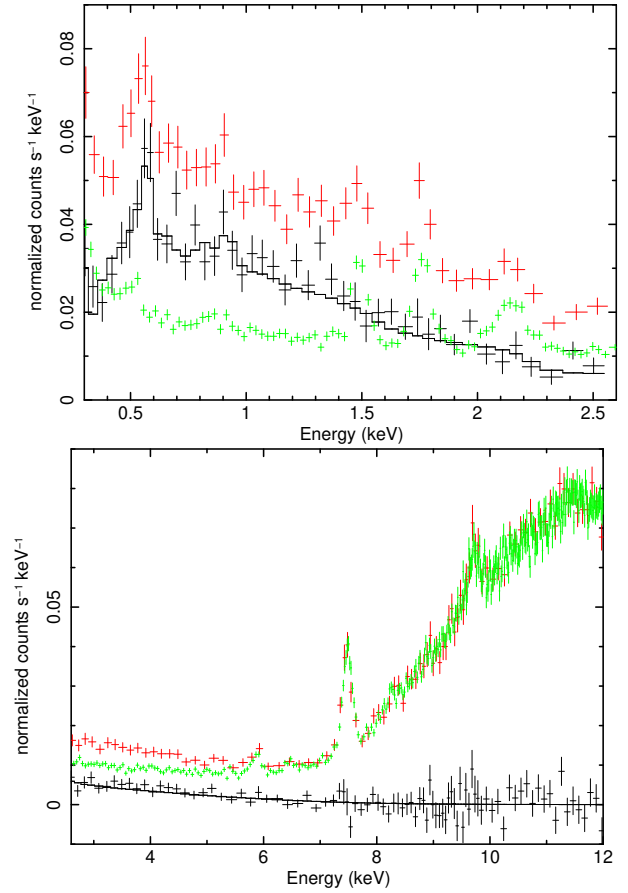


Fig. 2. | Same as Figure 1 for the XIS1 spectrum.

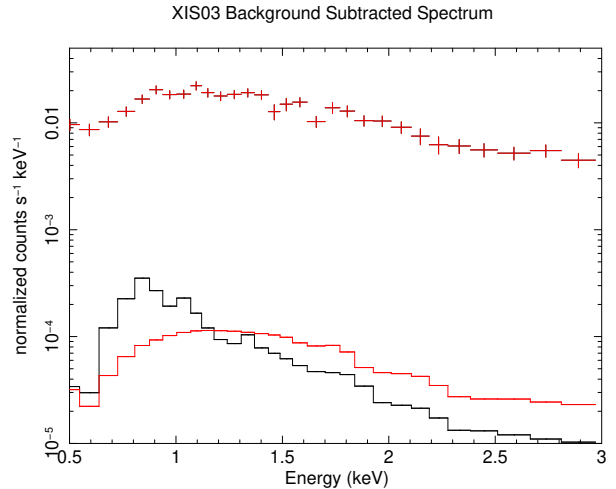


Fig. 3. | Background-subtracted XIS0+3 spectrum of Ursa Minor (crosses) compared with optimistic estimates of intrinsic X-ray emission from unresolved stellar sources (black histogram) and an AGN associate with an intermediate mass ($M_{\text{bh}} = 10^4 M_{\odot}$) black hole (red histogram).

these procedures, adding an “extra” line component and computing the line flux that results in an increase in χ^2 by some amount corresponding to the desired confidence level. The appropriate χ^2 may be chosen under the assumption of Gaussian statistics (in which case χ^2 is distributed as χ^2_q , where q is the number of parameters of

TABLE 1
Exposure Times and
Spectral Counts

| Detector | Time | Counts |
|----------|--------|--------|
| X IS0+ 3 | 138900 | 14170 |
| X IS1 | 69450 | 10610 |

interest) or based on simulations (Abazajian et al. 2007). Protassov et al. (2002) and others have identified shortcomings of this general approach, although some may be obviated by carrying out simulations.

We developed and applied a carefully considered alternative approach that we believe is statistically well founded. We do not subtract the NXB and use the unbinned data that is more appropriate for searches for a narrow, weak spectral line. Spectral fits must thus include an NXB component. Best fits are determined through minimization of the maximum likelihood Cash statistic (Cash statistic; Cash 1979), as appropriate for unbinned and unsubtracted data that obeys Poisson statistics, using version 12.4 of the XSPEC spectral fitting package¹¹.

A baseline model is constructed as follows. (1) We fit the generated NXB spectra (Section 2.2.2) over the full 0.4–12 keV band with a model consisting of two power-law components plus 10 narrow Gaussian lines with energies fixed at values given in the Suzaku technical description¹². X IS0+ 3 and X IS1 spectra are fitted independently at this stage. (2) Next, we partition the bandpass into five intervals (0.45–0.65 keV, 0.65–1.3 keV, 1.3–2.6 keV, 2.6–5.2 keV, 5.2– E_{max} keV, where $E_{\text{max}} = 10.4$ keV for X IS0+ 3 and 7.6 keV for X IS1) and refit each NXB spectral segment with the model described above (including only those lines that fall within the segment under consideration), allowing line energies and normalizations to freely vary. If fits are improved by the inclusion of additional lines, by the replacement of Gaussian with Lorentzian line profiles, or by introducing finite line widths, these adjustments are implemented. The partitioning results in two line-free (0.65–1.3 keV, 2.6–5.2 keV) and two line-rich segments (1.3–2.6 keV, 5.2– E_{max} keV) with total counts fairly evenly apportioned among these four (see Table 1 for total bandpass counts for each detector). (3) All 10 X IS0+ 3 and X IS1 NXB sub-spectra are then simultaneously fitted with line energies fixed at their locally determined values and one of the two power laws constrained to be the same for all spectra. This provides a phenomenological baseline NXB model. A baseline GXB + CXB model consists of an unabsorbed thermal plasma (apec) model, and variable abundance plasma (vpec) and power-law (plaw) models absorbed by the Galactic column density in the direction of Ursa Minor, as described in the previous section. The baseline NXB and GXB + CXB models are concatenated to form the total baseline model that we use as a starting point for our ultimate best fits. The best-fit vpec component requires a sub-solar oxygen abundance (all other elements are consistent with solar abundances and fixed

as such.

The total Ursa Minor spectra are likewise partitioned into 10 segments (five each for X IS0+ 3 and X IS1). The baseline model is applied and then new simultaneous fits to the 10 spectra are found by minimizing the Cash statistic. All NXB line energies and one NXB power-law component spectral index are now fixed; all constrainable parameters for the GXB (two temperatures, one oxygen abundance, two normalizations) and CXB (one power-law index, one normalization) components may freely vary but are tied for all 10 spectral segments since they are best determined globally. GXB + CXB model components differ only by a constant multiplicative scale factor for X IS1 relative to X IS0+ 3, to allow for residual flux cross-calibration offsets. All NXB line fluxes, one power-law index and two power-law norms are allowed to independently vary in each spectral segment for each detector (allowing both power-law indices to vary independently did not improve the fits). Back-fitting the best-fit GXB + CXB model components to the NXB-subtracted spectra described above yields acceptable fits; however, this is not the case when fitting the estimated NXB spectra with the best-fit NXB components. Evidently there are non-negligible (for our purposes) differences between the estimated and true NXB. These are apparent as residuals above 4 keV in the NXB-subtracted spectra (these residuals do not ruin global fits because of the relatively small number of > 4 keV source counts), and introduce systematic effects in the standard approach that we automatically account for in our analysis. When considering the inclusion of an additional (sterile neutrino) emission line, allowing the full range of NXB + GXB + CXB parameters of interest to vary provides a relatively conservative limit, while also utilizing unbinned, unsubtracted spectra enables us to consider energies for the extra line up to 10 keV (in X IS0+ 3). The issue of placing upper confidence limits on a quantity bounded from below (Feldman & Cousins 1998; Protassov et al. 2002) is mitigated since we can allow line fluxes to go negative without the total spectrum falling below zero.¹³

2.2.3. Spectral Fits

The best-fit NXB + GXB + CXB model to the Ursa Minor spectrum constitutes the null hypothesis that the X-ray spectrum consists solely of background components, to which we wish to test the hypothesis that an additional narrow¹⁴ emission line (presumably from sterile neutrino radiative decay) may be present. We emphasize that the spectra are minimally processed (screened of spurious events, but extended to the maximum useful bandpass, and unbinned and unsubtracted).

The final model has 62 parameters as follows: the 8 GXB + CXB parameters described above (including the X IS1/X IS0+ 3 multiplicative offset) and 54 NXB param-

¹³ The "slice method", wherein the total spectrum is partitioned into slices corresponding to the appropriate energy resolution, and the total counts in each slice used to derive an upper limit (Riemer-Sørensen, Hansen, & Pedersen 2006) may provide a yet more conservative limit. This method, unnecessarily in our view, discards well-established characteristics of known X-ray emission components.

¹⁴ Dwarf spheroidal dark matter velocity dispersions, 10–30 km s⁻¹, are much less than the XIS energy resolution.

¹¹ <http://heasarc.gsfc.nasa.gov/docs/xanadu/xspec/>

¹² http://heasarc.gsfc.nasa.gov/docs/suzaku/prop_tools/suzaku_td/suzaku_td.html

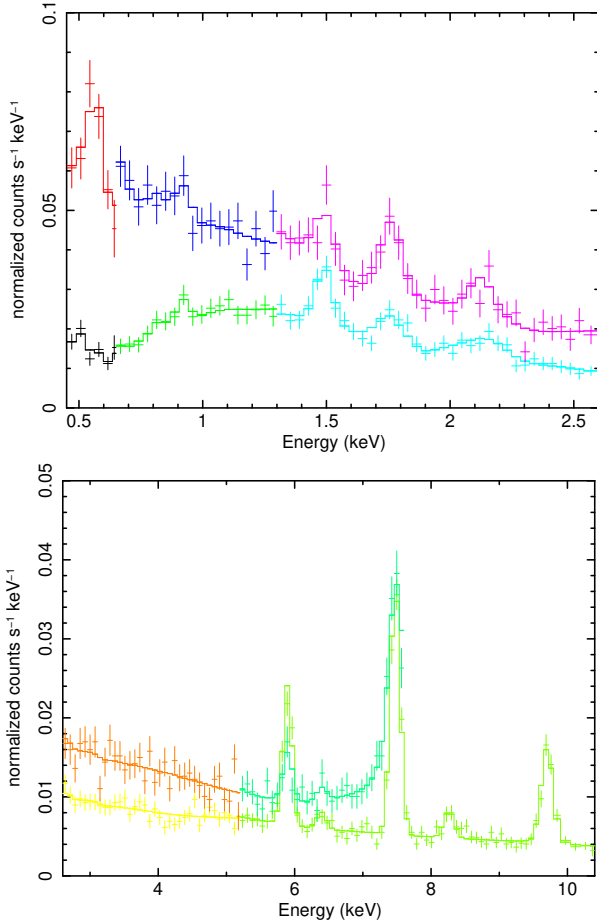


Fig. 4. | Low-energy (< 2.6 keV; above) and high-energy (> 2.6 keV; below) X IS0+3 and X IS1 spectra; the X IS1 spectrum has the higher count rate. Each spectrum is divided into five segments, delineated here by different colors, and all ten segments are simultaneously fitted as described in the text. Histograms trace the best-fit model.

eters { one power-law index and two power-law normalizations for each of the 10 spectra, nine emission line normalizations for each detector, plus two additional lines for X IS0+3 with energies above the X IS1 maximum energy of 7.6 keV, and two line widths for each detector. The best fit (Figure 4) has a minimized C -statistic of 2863 for 2879 bins (2817 degrees of freedom); best fit parameters are displayed in Tables 2 and 3 for GXB+CXB and NXB parameters, respectively (in the former the X IS1/X IS0+3 factor was found to be 1:1). Parameters are consistent with previous work (Matsuhashita et al. 2007; Takei et al. 2007; Sato et al. 2008; Werner et al. 2008) within their established variation on the sky as well as with the best fits to NXB-subtracted spectra of Ursa Minor described above.

2.3. Sterile Neutrino Emission Line Flux Upper Limits

The null hypothesis asserts that the Ursa Minor X-ray spectrum consists solely of background (NXB, GXB, CXB) components, with estimated parameters corresponding to the minimum value of the C -statistic (C_{null}). We may add a narrow (sterile neutrino radiative decay) line and independently re-fit the augmented model to obtain $C_{\text{line}}(E_{\text{line}})$ for a range of line energies E_{line} . Given the large number of counts in our unsubtracted spec-

TABLE 2
Best Fit CXB+GXB Parameters

| Model | kT or | O Abundance | Norm |
|-------|-------|-------------|---------|
| apec | 0.075 | | 0.0058 |
| vapac | 0.22 | 0.21 | 0.0016 |
| plaw | 1.45 | | 0.00087 |

Note. | Temperatures in keV; oxygen abundances relative to solar (Anders & Grevesse 1989); plasma model norms in units of $10^{14} \int D V n_e n_h = 4 d^2$, where d is the source distance in cm and n_e and n_h are the electron and hydrogen densities in cm^{-3} ; power-law norm in units of photons $\text{keV}^{-1} \text{cm}^{-2} \text{s}^{-1}$ at 1 keV (corresponding to $6.08 \times 10^9 \text{ erg cm}^{-2} \text{s}^{-1}$ over the 2-10 keV band). Norms correspond to a $20''$ circular region, that is, $1256.6 \text{ sq-arcmin} = 0.0001063 \text{ str}$.

tra, $C = C_{\text{null}} + C_{\text{line}}(E_{\text{line}})$ is ideally expected to be distributed as the χ^2 statistic with one degree of freedom, and the confidence level that a line is detected by $P(\chi^2_1 < C)$ (Kurczynski et al. 2000). In the absence of a significant detection, an upper limit line flux is that which corresponds to a value of C such that $P(\chi^2_1 < C) = \alpha$ (Yaqoob 1998).

We perform Monte Carlo spectral simulations in order to test how accurately these expectations are realized. The parameters from the best-fit null hypothesis model to the observed data are used to generate fake spectra that are re-fitted with the null hypothesis model. These second generation fits are used as seeds for subsequent Monte Carlo realizations (Butler et al. 2005; Markowitz et al. 2006; Porquet et al. 2007) that are generated and fitted in a manner that matches the actual spectra and their best fits (same exposure times and instrument responses, same assignment of fixed, tied, and free parameters). Fitting these simulated spectra with the null hypothesis model determines the minimized C -statistic C_{null} . Each simulated data set is additionally re-fitted with models that include an additional line at an (non-fixed) energy E_{line} that is stepped through the analysis bandpass (at 25 eV intervals) to determine the minimum C -statistic $C_{\text{line}}(E_{\text{line}})$ for each E_{line} . 1000 simulated spectra are generated for each hypothesis (null or null-plus-line-at- E_{line} for each E_{line}). The cumulative probability distribution $P(< C)$, where again $C = C_{\text{null}} + C_{\text{line}}(E_{\text{line}})$, yields an experimental estimate of the corresponding probability of rejecting the null hypothesis. The upper limit may then be estimated as described above, using the experimental, instead of χ^2_1 distribution. We find that $P(< C)$ matches $P(< \chi^2_1)$ only in spectral intervals with high total count rates and low NXB (i.e., in NXB-line-free regions). The joint distribution over all energies is well-approximated by $P(< \chi^2_2)$, and at no energies does $P(< C)$ fall below $P(< \chi^2_3)$ (Figure 5).

We adopt $C = 10$ upper limits. This corresponds to $P(< C) = 0.99$ in the joint distribution; at no energy was $P(C < 10)$ less than 0.984 (or greater than 0.996). The $C = 10$ upper and lower limits are plotted in Figure 6. Since no lower limit is > 0 , we infer that there is no line detected at 99% confidence. To derive limits in

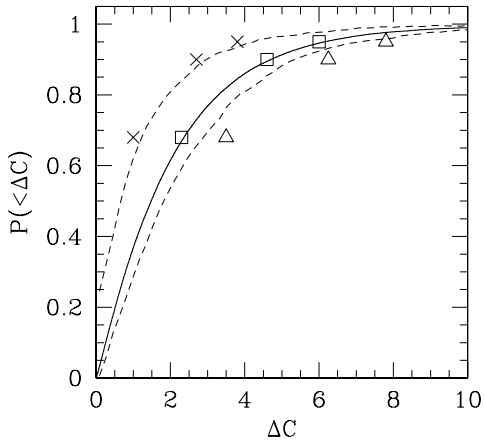


Fig. 5. Cumulative probability of $C = C_{\text{null}} + C_{\text{line}}$ from simulations. The solid curve shows the sum over all energies, while the broken curves show the full range spanned by simulations at individual energies. C crosses, boxes, and triangles show the 68, 90, and 95% cumulative probabilities for the χ^2_1 , χ^2_2 , and χ^2_3 distributions, respectively.

the vicinity of NXB lines we fix their line fluxes (otherwise, in fits and simulations, these are free to vary) at their best-fit values. The resulting limits are very nearly equal to the $C = 10$ uncertainty in the NXB line fluxes and, as they neglect any systematic errors in the NXB line strengths, will underestimate the upper limit of any additional emission line with precisely the same energy as the background features. The limits are tightest in spectral intervals where lines from the NXB and GXB are sparse or absent (especially $2 - 5$ keV). When we compare these limits to those more conventionally derived from the binned, background-subtracted spectra, we find that the $C = 10$ limits roughly correspond to $\chi^2 = 7$ in the < 4 keV region where the NXB is small or cleanly subtracts out.

3. LIMITS ON STERILE NEUTRINO PARAMETERS

The integrated line flux from sterile neutrinos decaying at rate $\Gamma_{\text{st}} = 10^{-27} \text{ s}^{-1}$ from a dark matter mass in projection of $10^7 M_\odot$ at a distance $100 d_{100}$ kpc is

$$F_{\text{line}} = 7.5 \cdot 10^{15} \cdot \Gamma_{\text{st}} \cdot M \cdot d_{100}^2 \text{ erg cm}^{-2} \text{ s}^{-1}; \quad (2)$$

where f_{st} is the dark matter fraction in sterile neutrinos. The corresponding number flux of $E = m_{\text{st}}/2$ photons from decays of particles with mass m_{st} that make up the total mass $10^7 M_\odot f_{\text{st}}$ is given by

$$F_{\text{line}} = 9.4 \cdot 10^6 \cdot \Gamma_{\text{st}} \cdot M \cdot d_{100}^2 \cdot \frac{\text{keV}}{m} \quad (3)$$

$$= 5.3 \cdot 10^{10} \cdot \frac{\sin^2}{10^{-10}} \cdot \frac{m_{\text{st}}}{\text{keV}}^4 \cdot f_{\text{st}} \cdot M \cdot d_{100}^2 \quad (4)$$

$\text{cm}^{-2} \text{ s}^{-1}$, where we have used the expression for Γ_{st} introduced in equation (1).

One can use this relation to set limits on sterile neutrino mass and mixing angle using the photon flux limits shown in Figure 6. The dark matter halo mass distribution in Ursa Minor may be estimated

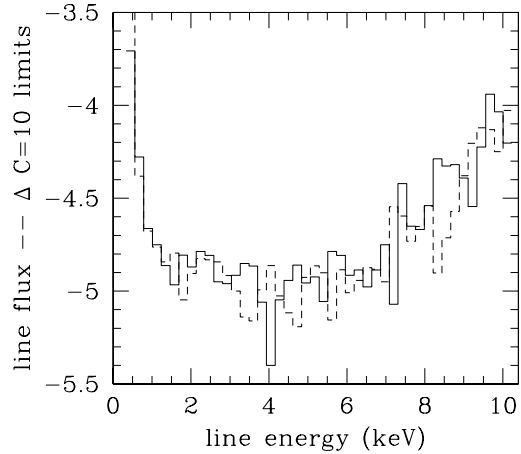


Fig. 6. Log of $C = 10$ line flux upper limits in photons $\text{cm}^{-2} \text{ s}^{-1}$ (solid histogram). Also shown is the log of the absolute value of the lower limits (that are all negative; broken histogram).

using stellar dynamics. Strigari and collaborators (Strigari et al. 2007a,b, 2008a,b) applied maximum likelihood analysis to constrain the parameters of a generalized Navarro-Frenk-White (NFW) profile (Diemand et al. 2005). Based on their confidence region for an NFW model (inner dark matter density slope of -1) in Strigari et al. (2008a), and the general integrated constraints (Gilmore et al. 2007; Wu 2007; Strigari et al. 2007b; Penarrubia, McConnachie, & Navarro 2008; Strigari et al. 2008b), the projected mass of Ursa Minor within $20''$ (0.4 kpc at our adopted distance of 69 kpc; Gallagher, & Harbeck 2003) is well determined from the projection of the NFW model (Bartelmann 1996; Golse & Kneib 2002; Yang, Mo, & Kaufmann 2003) to be $\sim 6 \cdot 10^7 M_\odot$. This is consistent with the weighted average derived from the estimates in the papers quoted above (Figure 7; these adopt various assumptions about the cusps of the profile) that has a variance of $\sim 25\%$, although the range of models formally allowed in Strigari et al. (2008a) spans factors of ~ 2 in either direction at that radius. The corresponding excluded dark matter decay rate Γ_{st} (for $f_{\text{st}} = 1$), derived from the $C = 10$ line flux upper limits, is shown in Figure 8 for line energies $0.45 < \text{keV} < 10.4$.

If one assumes that all the relic sterile neutrinos are produced via the DW mechanism, the absence of line emission from Ursa Minor provides an upper limit on the mixing angle as a function of mass that is independent of whether there are additional production mechanisms (which could only increase the abundance). The flux from equation (4), calculated for a given value of f_{st} , should not exceed the photon flux shown in Figure 6. In a given cosmological scenario, if the sterile neutrino relic abundance is a monotonic function of mass and mixing angle, $f_{\text{st}} = p(\sin^2 \theta; m_{\text{st}})$, then the region allowed in the $\sin^2 \theta - m_{\text{st}}$ plane is given by

$$\sin^2 \theta_{\text{max},p} = \min(\sin^2 \theta_{\text{max},1}; \sin^2 \theta_{\text{max},2}); \quad (5)$$

where $\sin^2 \theta_{\text{max},1}$ is determined from $f_{\text{st}} = p(\sin^2 \theta; m_{\text{st}}) < 1$ and $\sin^2 \theta_{\text{max},2}$ from the require-

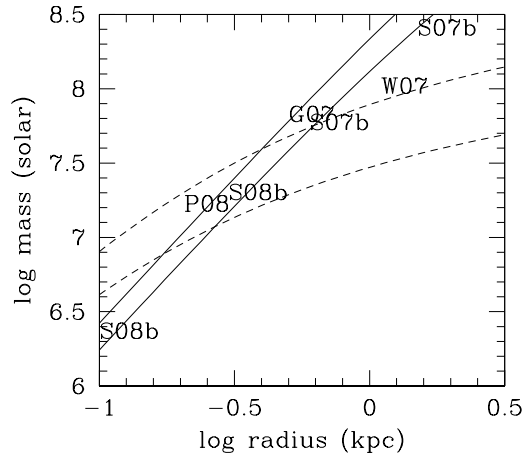


Fig. 7. Solid (broken) curve shows the 90% confidence limits of the least (most) compact mass profile from Strigari et al. (2008a). Also shown are estimates, at various radii from Gilmore et al. (2007) (G07), Wu (2007) (W07), Strigari et al. (2007b) (S07b), Penarrubia, McCannachie, & Navarro (2008) (P08), and Strigari et al. (2008b) (S08b).

ment that the flux in equation (4) not exceed the observed flux shown in Figure 6.

We derive two different limits that provide answers to the following questions: (1) whether the existence of a sterile neutrino with a given mass and mixing angle is consistent with standard cosmological history and (2) whether sterile neutrinos of a given mass and mixing angle can account for 100% of dark matter. These two constraints are, of course, different.

For the first limit, we take $f_{st} = p_{DW}(m_{st}; \theta)$ to be a function of mass and mixing angle and we assume the DW production mechanism, which gives the minimal abundance of sterile neutrinos in standard Big Bang cosmology. Aka, Laine, & Shaposhnikov (2007) provided fitting formulae for sterile neutrino abundance produced by the DW mechanism of the form

$$p_{DW}(\sin^2 \theta; m_{st}) = \frac{\sin^2 \theta}{10^{-10}} \frac{m_{st}}{1 \text{ keV}}; \quad (6)$$

as well as pairs $(\theta; m_{st})$ for average, minimum, and maximum production that account for hadronic uncertainties. The excluded region in the m_{st} plane, for production dominated by the DW mechanism, is given by equation (4), with

$$\frac{\sin^2 \theta_{max;1}}{10^{-10}} = \frac{1}{1 \text{ keV}} \frac{m_{st}}{1 \text{ keV}}; \quad (7)$$

and

$$\sin^2 \theta_{max;2} = (\sin^2 \theta_{max;1} \sin^2 \theta_{max;0} [1])^{1/2}; \quad (8)$$

where $\sin^2 \theta_{max;0} [1]$ is determined by setting $f_{st} = 1$. The resulting exclusion region is shown in Figure 9 for the minimal rate of DW production consistent with the results of Aka, Laine, & Shaposhnikov (2007), which provides the most conservative constraints. This region is excluded regardless of the physics responsible for mass

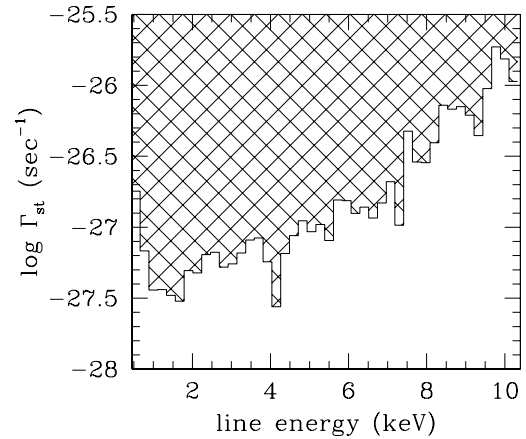


Fig. 8. Excluded dark matter radiative decay rates (hatched region) as a function of energy averaged over the inner 0.4 kpc of Ursa Minor, assuming that 100% of the dark matter is composed of sterile neutrinos ($f_{st} = 1$).

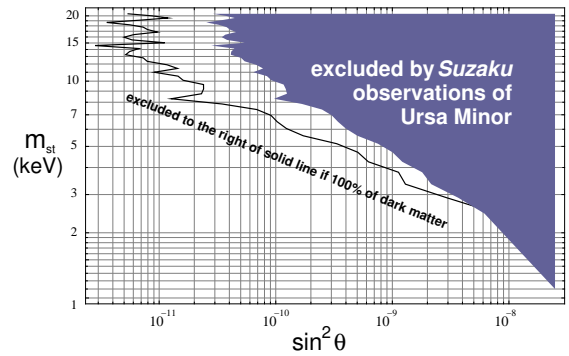


Fig. 9. Sterile neutrino parameter space to the right of the solid curve is excluded by the Suzaku observation of Ursa Minor if dark matter is solely composed of sterile neutrinos produced by some (unspecified) mechanism. The solid exclusion region is model-independent, based only on the assumption of the standard cosmological history below the temperature of a few hundred MeV, when the DW production by neutrino oscillations takes place.

generation of neutrinos or any other physics beyond direct mixing between sterile and active neutrinos.

For the second kind of limit, we determine the part of parameter space for which sterile neutrinos can account for all the cosmological dark matter, while still being consistent with Suzaku observations. Here we set $f_{st} = 1$ without reference to any specific production mechanism. The excluded region (for $f_{st} = 1$) corresponding to the $C = 10$ upper limits on $f_{st} f_{st}$ shown in Figure 8 is delineated by the solid line in Figure 9. Sterile neutrinos occupying the parameter space to the right of the solid line cannot make up all of the dark matter (although such a particle may exist in nature, in contrast with the previous limit).

One can ask which dark-matter particle mass in the form of sterile neutrinos, for $f_{st} = 1$, produced solely by the DW mechanism is consistent with Suzaku observations. Here one can set an upper limit on the sterile neutrino mass: $m_{st} < 2.5 \text{ keV}$. However, the DW mechanism with $f_{st} = 0.1$ is not ruled out at any energy covered

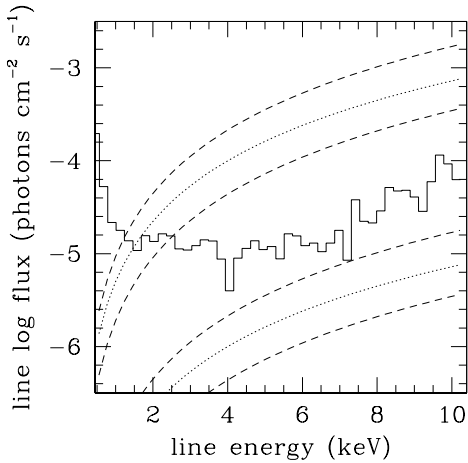


Fig. 10. Line flux upper limits from Figure 6 re-plotted with the $f_{st} = 1$ (upper curves) and $f_{st} = 0.1$ (lower curves) DW predictions for maximum, average, and minimum production by the Suzaku spectra ($1-20$ keV). This is shown in Figure 10, where our line flux upper limits are compared with the DW predictions.

3.1. Comparison to Previous Work

Because different criteria for estimating line flux upper limits are used, a precise comparison with previous results is difficult. Our limits are about a factor of 3 better than those for Ursa Minor in Boyarsky, Nevalainen, & Ruchayskiy (2007) over the overlapping bandpass. The constraints shown in Figure 9 are comparable to the combined constraints from the Milky Way (Boyarsky, Nevalainen, & Ruchayskiy 2007) and M 31 (Boyarsky et al. 2008), and slightly tighter than those from the unresolved Chandra CXB (Abazajian et al. 2007) and from the “bullet” cluster, 1E 0657-56 (Boyarsky, Ruchayskiy, & Markevitch 2008). Asaka, Laine, & Shaposhnikov (2007) compiled and plotted various X-ray limits on the combination of m_{st} and $\sin^2 2\theta$. We attain a comparable level of sensitivity over the entire 1-20 keV mass range with a Suzaku observation of a single object.

4. DISCUSSION, CONCLUSIONS, AND FUTURE PROSPECTS

With a single Suzaku observation of the Ursa Minor dwarf spheroidal, we have derived limits on the mass and mixing angle of the sterile neutrino dark matter candidate that are comparable to or better than previous constraints. These limits are illustrated in Figure 9 for the case where sterile neutrinos comprise all of the dark matter regardless of how they are produced in the early universe and, in the more general case, when their abundance is not assumed, but is calculated under the assumptions that minimize it. The best estimate of the total projected dark matter mass within 400 pc of $6 \cdot 10^7 M_{\odot}$ is adopted here. If solely produced by the DW mechanism, sterile neutrinos cannot constitute 100% of the dark matter in Ursa Minor unless they are less massive than 2.5 keV.

Because of its orbit, Suzaku has a lower and more stable background than either the Chandra or XMM-Newton Observatories, and its spectrometers have sharper energy resolution. Our approach in deriving limits utilizes the C-statistic to evaluate a very general model fit to the data with minimum pre-processing and no background subtraction. Thus, there are no a priori assumptions about the accuracy of the NXB estimate that we only use to set line energies and shapes, or whether an extra line feature lies above or below the total continuum. Our final limits are those that correspond to a change in the C-statistic that occurred in 1% of our Monte Carlo simulations. These factors may account for why our constraints represent only modest improvements over previously published limits despite the more optimal characteristics of Suzaku. As the NXB characterization improves, it may be possible to tighten upper limits in the $m_{st} > 2$ keV regime; at lower masses, the ubiquity of the GXB will remain a barrier until significantly higher energy resolution is attained (e.g., with Astro-H¹⁵).

Since there is some uncertainty as to the dynamical state of dwarf spheroidals on an individual basis, X-ray constraints obtained from additional systems are warranted (e.g., our paper in preparation on the Suzaku observation of the Draco system). The Sloan Digital Sky Survey (SDSS) has approximately doubled the number of galaxies identified with the local group population and revealed a new sub-population of faint Milky Way satellites (Belokurov et al. 2007), including some with very high mass-to-light ratio (Strigari et al. 2008a,b) that may provide the best targets for investigations of this type.

Finally, predictions of the Ly forest power spectrum in fully self-consistent large-scale structure simulations with sterile neutrinos can provide complementary constraints in the form of a lower limit on the particle mass.

Sterile neutrinos remain a viable dark matter candidate. For example, a sterile neutrino with a mass of $m_{st} = 4$ keV and $\sin^2 2\theta = 4 \cdot 10^{-10}$ could account for all of the dark matter (or 15%–75% if produced solely by the DW mechanism) and explain pulsar kicks (Kusenko, Mandal, & Mukherjee 2008) without violating the line flux upper limits.

This research has made use of data obtained from the Suzaku satellite, a collaborative mission between the space agencies of Japan (JAXA) and the USA (NASA). ML thanks R. M. Ushotzky for providing the initial impetus for this project; U. Hwang, K. Hamaguchi, and A. M. Arkowitz for advice and assistance with data analysis; he dedicates this paper to the memory of E. Boldt for many years of collaboration and conversation on the connections between particle physics and astrophysics. The work of ML was supported by NASA grants NNX08AD96G and NNX07AO94G. The work of AK was supported in part by DOE grant DE-FG03-91ER40662 and by NASA ATFP grant NNX08AL48G. Support for PLB has come from the AUGER membership and theory grant 05CU5PD1/2 via DESY/BMBF and VIKOS.

¹⁵ http://www.isas.ac.jp/e/enterp/m_issions/astro-h/index.shtml

REFERENCES

- Abazajian, K. N. 2006a, *Phys. Rev. D*, 73, 063506
 Abazajian, K. N. 2006b, *Phys. Rev. D*, 73, 063513
 Abazajian, K., Fuller, G. M., & Patel, M. 2001, *Phys. Rev. D*, 64, 023501
 Abazajian, K., Fuller, G. M., & Tucker, W. H. 2001, *ApJ*, 562, 593
 Abazajian, K., & Koushiappas, S. M. 2006, *Phys. Rev. D*, 74, 023527
 Abazajian, K. N., Markevitch, M., Koushiappas, S. M., & Hickox, R. C. 2007, *Phys. Rev. D*, 75, 063511
 Anders, E., & Grevesse, N. 1989, *Geochimica et Cosmochimica Acta* 53, 197
 Asaka, T., Shaposhnikov, M., & Laine, M. 2007, *J. High Energy Phys.*, 01, 091
 Barger, V., Phillips, R. J. N., & Sarkar, S. 1995, *Physics Letters B*, 356, 617
 Bartelmann, M. 1996, *A & A*, 313, 697
 Belokurov, V., et al. 2007, *ApJ*, 654, 897
 Biemann, P. L., & Kusenko, A. 2006, *Phys. Rev. Lett.*, 96, 091301
 Boyanovsky, D. 2008 *Phys. Rev. D*, 78, 103505
 Boyarsky, A., Iakubovskiy, D., Ruchayskiy, O., & Savchenko, V. 2008, *MNRAS*, 387, 1361
 Boyarsky, A., Lesgourgues, J., Ruchayskiy, O., & Viel, M. 2009, *J. Cosmology Astropart. Phys.*, 5, 012
 Boyarsky, A., Neronov, A., Ruchayskiy, O., & Shaposhnikov, M. 2006a, *MNRAS*, 370, 213
 Boyarsky, A., Neronov, A., Ruchayskiy, O., & Shaposhnikov, M. 2006b, *Phys. Rev. D*, 74, 103506
 Boyarsky, A., Neronov, A., Ruchayskiy, O., Shaposhnikov, M., & Tkachev, I. 2006c, *Phys. Rev. Lett.*, 97, 261302
 Boyarsky, A., Nevalainen, J., & Ruchayskiy, O. 2007, *A & A*, 471, 51
 Boyarsky, A., Ruchayskiy, O., & Markevitch, M. 2008. *ApJ*, 673, 752
 Butler, N., Ricker, G., Vanderspek, R., Ford, P., Crew, G., Lamb, D. Q., & Jemigan, J. G. 2005, *ApJ*, 627, L9
 Cash, W. 1979, *ApJ*, 228, 939
 Diemand, J., Zemp, M., Moore, B., Stadel, J., & Carollo, C. 2005, *MNRAS*, 364, 665
 Odellson, S., & Widrow, L. M. 1994, *Phys. Rev. Lett.*, 72, 17
 Dolgov, A. D. 2002, *Phys. Rept.*, 370, 333
 Dolgov, A. D., & Hansen, S. H. 2002, *Astroparticle Physics*, 16, 339
 Feldman, G. J., & Cousins, R. D. 1998, *Phys. Rev. D*, 57, 3873
 Ferrarese, L., & Ford, H. 2005, *Space Sci. Rev.*, 116, 523
 Fuller, G. M., Kusenko, A., Mocciiu, I., & Pascoli, S. 2003, *Phys. Rev. D*, 68, 103002
 Fryer, C. L., & Kusenko, A. 2006, *ApJS*, 163, 335
 Gao, L., & Theuns, T. 2007, *Science*, 317, 1527
 Gebhardt, K., et al. 2000, *ApJ*, 539, 13
 Gilmore, G., Wilkinson, M. I., Wyse, R. F. G., Kleyna, J. T., Koch, A., Evans, N. W., & Grebel, E. K. 2007, *ApJ*, 663, 948
 Graham, A. W. 2008a, *ApJ*, 680, 143
 Graham, A. W. 2008b, *PASA*, 25, 167
 Greene, J. E., Ho, L. C., & Barth, A. J. 2008, *ApJ*, 688, 159
 Golse, G., & Kneib, J.-P. 2002, *A & A*, 390, 821
 Grebel, E. K., Gallagher, J. S., III, & Harbeck, D. 2003, *AJ*, 125, 1926
 Haring, N., & Rix, H.-W. 2004, *ApJ*, 604, L89
 Hidaka, J., & Fuller, G. M. 2007, *Phys. Rev. D*, 76, 083516
 Ishisaki, Y., et al. 2007, *PASJ*, 59, S113
 Kadota, K. 2008, *Phys. Rev. D*, 77, 063509
 Koyama, K., et al. 2007, *PASJ*, 59, S23
 Kurczynski, P., et al. 2000, *ApJ*, 543, 77
 Kusenko, A. 2004, *J. Mod. Phys. D*, 13, 2065
 Kusenko, A. 2006, *Phys. Rev. Lett.*, 97, 241301
 Kusenko, A., Mandal, B. P., & Mukherjee, A. 2008, *Phys. Rev. D*, 77, 123009
 Kusenko, A., & Segre, G. 1997, *Phys. Lett. B*, 396, 197
 Laine, M., & Shaposhnikov, M. 2008, *JCAP*, 06, 31
 Maccarone, T. J., Fender, R. P., & Tzioumis, A. K. 2005, *MNRAS*, 356, 17
 Marconi, A., & Hunt, L. K. 2003, *ApJ*, 589, L21
 Markowitz, A., Reeves, J. N., & Braito, V. 2006, *ApJ*, 646, 783
 Matsushita, K., et al. 2007, *PASJ*, 59, S327
 Meiksin, A. A. 2009, *Rev. Mod. Phys.*, in press
 Mitsuda, K., et al. 2007, *PASJ*, 59, S1
 Munyaneza, F., & Biemann, P. L. 2005, *A & A*, 436, 805
 Munyaneza, F., & Biemann, P. L. 2006, *A & A*, 458, L9
 Nakajima, H., et al. 2008, *PASJ*, 60, S1
 Narayanan, V. K., Spergel, D. N., D'Avella, R., & Madau, P. 2000, *ApJ*, 543, L103
 Pal, P. B., & Wolfenstein, L. 1982, *Phys. Rev. D*, 25, 766
 Palazzo, A., Cummerbatch, D., Slosar, A., & Silk, J. 2007, *Phys. Rev. D*, 76, 103511
 Penarubia, J., Maccannachie, A. W., & Navarro, J. F. 2008, *ApJ*, 672, 904
 Petraki, K. 2008, *Phys. Rev. D*, 77, 105004
 Petraki, K., & Kusenko, A. 2008, *Phys. Rev. D*, 77, 065014
 Porquet, D., et al. 2007, *A & A*, 473, 67
 Protassov, R., van Dyk, D. A., Connors, A., Kashyap, V. L., & Siginovsky, A. 2002, *ApJ*, 571, 545
 Revinvtsev, M., Churazov, E., Sazonov, S., Forman, W., & Jones, C. 2008, *A & A*, 490, 37
 Reiser-Sørensen, S., Hansen, S. H., & Pedersen, K. 2006, *ApJ*, 644, L33
 Reiser-Sørensen, S., Pedersen, K., Hansen, S. H., & Dahle, H. 2007, *Phys. Rev. D*, 76, 043524
 Sato, K., et al. 2008, *PASJ*, 60, S333
 Serlemitsos, P. J., et al. 2007, *PASJ*, 59, S9
 Shaposhnikov, M., & Tkachev, I. 2006, *Physics Letters B*, 639, 414
 Shi, X. D., & Fuller, G. M. 1999, *Phys. Rev. Lett.*, 82, 2832
 Stasielak, J., Biemann, P. L., & Kusenko 2007, *ApJ*, 654, 290
 Strigari, L. E., Bullock, J. S., & Kapinghat, M., Diemand, J., Kuhlen, M., & Madau, P. 2007, *ApJ*, 669, 676
 Strigari, L. E., Koushiappas, S. M., Bullock, J. S., & Kapinghat, M. 2007, *Phys. Rev. D*, 75, 3526
 Strigari, L. E., Koushiappas, S. M., Bullock, J. S., Kapinghat, M., Simón, J. D., Geha, M., & Willman, B. 2008, *ApJ*, 678, 614
 Strigari, L. E., Bullock, J. S., Kapinghat, M., Simón, J. D., Geha, M., Willman, B., & Walker, M. G. 2008, *Nature*, 454, 1096
 Takei, Y., et al. 2007, *PASJ*, 59, S339
 Tawara, Y., et al. 2008, *PASJ*, 60, S307
 Tawa, N., et al. 2008, *PASJ*, 60, S11
 Tokoi, K., et al. 2008, *PASJ*, 60, S317
 Uchiyama, Y., et al. 2008, *PASJ*, 60, S35
 Uchiyama, Y., et al. 2009, *PASJ*, 61, S9
 Viel, M., Becker, G. D., Bolton, J. S., Haehnelt, M. G., Rauch, M., & Sargent, W. L. W. 2008, *Phys. Rev. Lett.*, 100, 041304
 Watson, C. R., Beacom, J. F., Yüksel, H., & Walker, T. P. 2006, *Phys. Rev. D*, 74, 033009
 Wemer, N., Finoguenov, A., Kaastra, J. S., Simionescu, A., Dietrich, J. P., Vink, J., & Böhringer, H. 2008, *A & A*, 482, 29
 Wilkinson, M. I., Kleyna, J. T., Evans, N. W., Gilmore, G. F., Irwin, M. J., & Grebel, E. K. 2004, *ApJ*, 611, L21
 Wu, X. 2007, *ApJ*, submitted (astro-ph/0702233v1)
 Yang, X. H., Mo, H. J., & Kaufmann, G. 2003, *MNRAS*, 339, 387
 Yaqoob, T. 1998, *ApJ*, 500, 89
 Zaritsky, D., Gonzalez, A. H., & Zabludov, A. 2006, *ApJ*, 638, 725

